≡P Science Press

ARTICLE

Phase Composition and Photocatalytic Properties of La³⁺-doped TiO₂ Nanopowders

Yan Jikang[1], Rong Xuequan[2], Gu Xin[1], Du Jinghong[1], Gan Guoyou[1]

[1] Kunming University of Science and Technology, Kunming 650093, China; [2] University of Science and Technology Beijing, Beijing 100083, China

Abstract: A sol-gel method was used to prepare La^{3+}-doped TiO_2 nanopowders. The sample was characterized with XRD, TEM, HRTEM, STEM-EDS, XPS and ultraviolet-visible (UV-Vis) spectroscopy. The changes of the La^{3+}-doped TiO_2 in the phase transition were discussed on the aspects of its phase composition, the average grain size, the microstructure, the chemical states and UV-Vis absorption spectroscopy. The results show that doping with La^{3+} significantly suppresses the phase change and grain growth of TiO_2. It effectively improves the TiO_2 dispersibility and reduces the average particle size of TiO_2. With the increase of the calcination temperature, the second phase $La_4Ti_{19}O_{24}$ gradually precipitates from the La^{3+}-doped TiO_2 and forms an incoherent interface with the brookite TiO_2 phase, which precipitates in the form of irregular spheres on the surface of the TiO_2 base. Secondary phases are originated from segregation of point defects La'_{Ti} at grain boundaries in La^{3+} doped TiO_2. The segregation driving force is mainly the elastic strain energy. With the increase of calcining temperature, the atomic fraction of the O_{1S} in the La^{3+}-doped TiO_2 gradually decreases, and that of the La_{3d} gradually increases. There is an energy loss peak at the higher binding-energy side of the main peak of the La_{3d}, and Ti^{3+} exists after the calcination. La^{3+} doping makes the optical absorption band edge of the TiO_2 red-shift. But with increasing the calcination temperature, the optical absorption bandedge blue shifts.

Key words: titanium dioxide; phase change; lanthanum; photocatalysis

---

TiO_2 has the characteristics of chemical stability, non-toxicity, and low cost. It is widely used in the fields such as photocatalysis, photovoltaic, and gas sensor[1-3]. However, its solar energy conversion efficiency is low. It is easy for the photo-generated electrons and holes to recombine, which restricts the further improvement of its photocatalytic activity[4]. In other words, the performance of TiO_2 is determined by its properties such as lattice type, specific surface area, dispersibility, and band structure. Wang et al[5] found that the mixed-type TiO_2 had better photocatalytic performance than the one with a single anatase phase in the study of the relationship between the phase change and the photocatalytic activity. But when the rutile phase was over a certain value, the photocatalytic activity decreased with the content increase of the rutile phase. The smaller the TiO_2

particle size and the bigger the specific surface area, the smaller the probability of the electron-hole recombination, and the higher the photocatalytic activity[6]. At the same time, due to their superhydrophilic properties, the TiO_2 particles easily aggregate under the van der Waals forces in liquid medium. In addition, TiO_2 has a wide energy band gap and only absorbs UV light, which are the shortcomings that significantly restrict its application.

At present, doping with rare-earth ions is one of the often used methods to improve the properties of TiO_2[6]. Yue et al[7] thought oxygen vacancies were generated when the rare-earth ions mainly with a single valence state or +3 valence states (for example, La^{3+}, Gd^{3+}, and Y^{3+}) substituted Ti^{4+} by diffusing into the lattice. It enhanced the phase change and grain growth of the rutile phase, and increased the photocatalytic activity of

---

the TiO_2 suspension system. For variable-valence rare-earth ions (for example, Ce^{4+}, Tb^{3+}, and Eu^{3+}), a redox reaction occurred at the surface of the TiO_2 lattice, which produced oxygen vacancies or interstitial titanium. Then, it further affected the photocatalytic activity. Ranjit et al[8] found that doping with rare-earth ions such as Eu^{3+}, Pr^{3+}, and Yb^{3+} suppressed the phase change of TiO_2 from anatase to rutile phase, and enhanced the photocatalytic degradation of organic compounds containing carboxyl groups to some extent.

It can be seen that the photocatalytic performance of TiO_2 powder was significantly affected by the lattice defects and surface effects generated by the factors such as the phase composition, the doping element, and the grain size[9]. However, scholars currently have been focusing on the research of the effect of chemical composition of TiO_2 on its photocatalytic performance. There is rarely any systematic report on the effect of ion doping on the changes of lattice type and grain size of the TiO_2 photocatalyst[10]. Hence, it has a certain guidance to adjust the TiO_2 performance by studying the mechanism and the controlling condition of the TiO_2 phase change[11].

In this work, a sol-gel method was used to make un-doped TiO_2 powders and doped TiO_2 powders with 5 mol% La^{3+}. The samples were characterized with XRD, TEM, STEM, STEM-EDS and UV-Vis absorption spectroscopy for the phase change process of the La^{3+}-doped TiO_2. Discussions were made on the changes of the phase composition, the microstructure, the chemical states and the optical absorption band edge in the phase transition of the La^{3+}-doped TiO_2. This work started from the phase change process of TiO_2. The effect of La^{3+} on the TiO_2 nanopowder was discussed to provide a basis for its applications in the field of photocatalysis.

1 Experiment

1.1 Sample preparation

At first, solutions A and B were prepared as follows. For the type A, 3 mL concentrated nitric acid, 9 mL deionized water and 50 mL ethanol were mixed. And 25 mL tetrabutyl titanate and 50 mL ethanol were mixed as the type B.

When preparing the un-doped TiO_2 powder, add the solution A drop by drop into the stirring B to form sol-gel, which was then aged for 48 h. The sol-gel was dried at 100 °C for another 48 h to have dry gel. Finally, the samples of the dry gel were calcified for 30 min at 400, 450, 500, 550 and 650 °C. The required un-doped TiO_2 powder was obtained after cooling in the furnace.

For the preparation of the La^{3+}-doped TiO_2 powder, 5 mol% La^{3+} was dissolved into the solution A to form the liquid D. Then the liquid D was added drop by drop to the stirring solution B to form sol-gel. The sol-gel was then aged for 48 h, and then dried for 48 h at 100 °C to become dry gel. At last, the samples of the dry gel were calcified for 30 min at 550, 650, 750, 800, 850 and 900 °C. The desired powder of TiO_2

doped with 5 mol% La^{3+} was obtained after cooling down in the furnace.

1.2 Sample measurements

1.2.1 X-ray diffraction (XRD)

An X-ray diffractometer (XRD, model D/max-2200) was used to analyze the phase transition temperature, the phase composition and the average grain size of the sample. The working voltage and the tube current of the XRD were 36 kV and 30 mA, respectively. The wavelength of the Cu Kα radiation was 0.1504 nm. The scanning speed was 10°/min.

The grain size was estimated with the Scherrer formula, which is expressed with the following:

$$D \approx \frac{0.9\lambda}{\beta\cos\theta} \quad (1)$$

In Eq.(1), D is the average grain size (nm), λ is the wavelength of the incident X-ray (0.1504 nm), β is the full-width-at-half-magnitude (FWHM) of the diffraction, and θ is the diffraction angle of the diffraction peak.

Using the R_i (the reference intensity) as the basis (called I/I_c value), the phase composition of the sample was calculated with Eq. (2)[12] according to the theory and method of R_i quantitative phase analysis:

$$X_i = \frac{I_i / R_i}{\sum_{i=1}^{n} I_i / R_i} \quad (2)$$

In Eq.(2), I_i is the measured relative intensity of the phase composite i, and X_i is the mass fraction of the composite i.

1.2.2 X-ray photoelectron spectroscopy (XPS)

A XPS (model PHI5000 Versaprobe-II) was used to analyze the change of the chemical states of the La^{3+}-doped TiO_2. The XPS was excited with an Al Kα radiation (1486.6 eV) at a power of 50 W. The C 1s (284.8 eV) of the carbon contamination was used for the charge correction of the binding energy (BE).

1.2.3 Transmission electron microscopy (TEM)

A field emission TEM with scanning transmission mode (STEM, model Tecnai G2 TF30 S-Twin) was used to conduct energy dispersive analysis (STEM-EDS) with the EDAX X-ray spectrometer installed on the machine.

A small amount of the powder to be measured was put in ethanol and shocked in an ultrasonic cleaning machine for 10 min to obtain the powder suspension for measurement. The suspension liquid was dropped onto a copper net strengthened with the carbon collodion membrane support. After drying, the sample was analyzed as follows. With the field-emission TEM (model Tecnai G2 TF30 S-Twin), the morphology was observed under the modes of TEM and high-resolution TEM (HRTEM). The morphology of the second phase was observed under the STEM mode. The STEM-EDS was used to characterize the elemental composition of the sample surface. The point resolution of the field emission TEM was 0.205 nm, and its line resolution was 0.102 nm, at an accelerating voltage of 300 kV.

1.2.4 UV-Vis spectrometer

A UV-Vis spectrometer (model U-4100) was used to analyze the absorption spectroscopy of the sample. The scanning wavelength range was 200~700 nm. The band gap of the sample was calculated by Eq.(3):

$$\lambda_g = \frac{1240}{E(\text{eV})} \tag{3}$$

2 Results and Discussion

2.1 Phase analysis

Fig.1 is the XRD patterns of the samples, while Table 1 shows their phase composition while Table 2 summarizes their average grain size. It can be seen from the combination of Fig.1, Tables 1 and 2 that the calcination temperatures of TiO$_2$ mainly locate in the range of 400~650 °C for the formation and completion of the rutile phase. The calcination temperatures of the La^{3+}-doped TiO$_2$ are mainly in the range of 750~900 °C. Doping with La^{3+} suppresses the phase transmission and grain growth of TiO$_2$, and 2.3 wt% of the second phase La$_4$Ti$_9$O$_{24}$ precipitates after calcination at 750 °C. The precipitation is a compound with La$_2$Ti$_2$O$_7$ as the principal crystalline phase. The second phase has pinning effect on the grain boundary and grain size, and blocks the movement of the TiO$_2$ grain boundaries. Hence, it suppresses the phase change of TiO$_2$[13].

2.2 Microstructure analysis

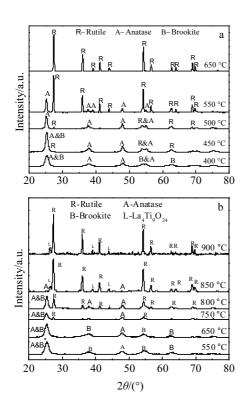Fig.2 is the TEM images of the un-doped TiO$_2$ after 550 °C

Table 1 Phase composition of the sample

Sample	Calcination temperature/°C	Content/wt%			
		Brookite	Anatase	Rutile	La$_4$Ti$_9$O$_{24}$
TiO$_2$	400	42.6	57.4	0	
	450	40.8	57.8	1.4	
	500	0	87.3	12.4	
	550	0	34.1	65.9	
	650	0	0	100	
La^{3+}-TiO$_2$	550	70.1	29.9	0	0
	650	42.5	57.5	0	0
	750	33.3	46.7	17.7	2.3
	800	20.1	42.3	34	3.6
	850	0	9.3	68	22.7
	900	0	0	72.2	27.8

Table 2 Average grain size of the sample

Sample	Calcination temperature/°C	Crystallite size/nm			
		Brookite	Anatase	Rutile	La$_4$Ti$_9$O$_{24}$
TiO$_2$	400	14.7	8.8	-	
	450	25.6	27.5	-	
	500	-	15.8	28.2	
	550	-	25.9	43.5	
	650	-	-	45.7	
La^{3+}-TiO$_2$	650	10.1	10.1	-	-
	750	11.1	11.1	25.9	-
	800	-	16.5	27.6	-
	850	-	-	26.1	21.5
	900	-	-	40.4	

Fig.1 XRD patterns of the samples: (a) TiO$_2$ and (b) La^{3+}-doped TiO$_2$
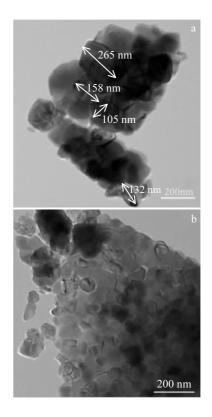

Fig.2 TEM images of the un-doped TiO$_2$ calcinated at 550 °C

calcination. Fig.2a shows that the average particle size of the un-doped TiO_2 is 165 nm. Fig.2b indicates many small grains aggregate to form a big particle for the un-doped TiO_2, which is due to the superhydrophilicity of TiO_2 itself. TiO_2 particles easily aggregate under the van der Waals forces in the liquid medium.

Fig.3 is the TEM images of the La^{3+}-doped TiO_2 after calcination at 750 °C. In Fig.3a, the bigger particle of the La^{3+}-doped TiO_2 has an average size of 79 nm, showing the significant decrease in the average particle size of the La^{3+}-doped TiO_2. It can be seen from Figs.3a~3c that the particle size of the La^{3+}-doped TiO_2 has a non-uniform distribution. Since the activation energy of the reaction is bigger for a small particle than for the big one, the transformation from the anatase phase to the rutile phase can occur at a lower temperature for small particles. The phase change of a big particle can only happen at higher temperatures[14]. Therefore, the phase change process of the La^{3+}-doped TiO_2 occurs in a wide range of temperatures. Fig.3d indicates the dispersibility of the La^{3+}-doped TiO_2 is significantly improved. It is the pinning effect of the second phase on the grain boundary and the grain size that suppresses the movements of the TiO_2 grain boundaries, which improves the TiO_2 dispersibility[15].

Fig.4 is the HRTEM images and SAED patterns of the La^{3+}-doped TiO_2 calcinated at 750 °C. In Fig. 4a, the crystal plane distance is shown as 0.211 and 0.240 nm, and the crystal surface corresponds to the (5111) and (152) planes of $La_4Ti_9O_{24}$.

The crystal planes with the interplanar distance of 0.240 and 0.346 nm correspond to (131) and (111) planes of the brookite TiO_2, respectively. Therefore, the $La_4Ti_9O_{24}$ phase with a crystal zone axis $[\bar{1}79\,\bar{1}4]$ and the brookite TiO_2 with a crystal zone axis $[\bar{1}01]$ forms an incoherent interface. In Fig.4b, the brookite has (111) and (131) faces, while the $La_4Ti_9O_{24}$ has (004), (400), (771), $(46\bar{2})$, (152) and (5111) faces. The planes with an interplanar distance of 0.187, 0.357 and 0.363 nm are the (771), (400), and (004) planes of $La_4Ti_9O_{24}$.

It can be seen that it is easy for $La_4Ti_9O_{24}$ to form an incoherent interface with the brookite TiO_2. The $La_4Ti_9O_{24}$ and brookite TiO_2 belong to the orthorhombic system with a large mismatch between their lattice constant. In order to lower the interface energy at the incoherent interface, $La_4Ti_9O_{24}$ will precipitate at the interface.

Fig.5 includes the STEM-EDS images of the La^{3+}-doped TiO_2 calcinated at 750 °C. Figs.5a, 5c, and 5e are the STEM images from the field-emission TEM under the scanning transmission mode. The STEM image has atomic number contrast. Therefore, Fig.5b, 5d and 5f are obtained from the analyses of the energy spectrum at the bright spots and dark spots. In Fig. 5, the atomic percentage content of La in the dark area is low, which indicates the La-Ti-O bond is formed when La^{3+} enters TiO_2 in the calcination process.

It is known when connecting with the XRD results that the bright area in Fig.5 is the second phase $La_4Ti_9O_{24}$. It is precipitated as irregular spheres on the surface of the base TiO_2. It is
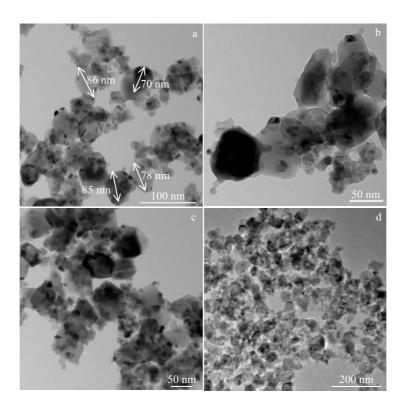

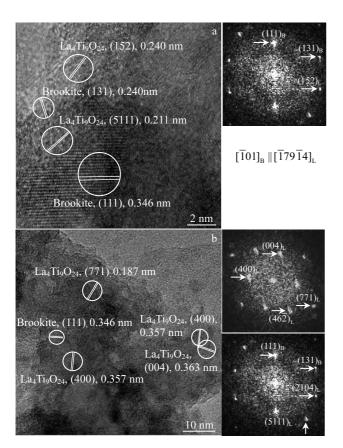Fig.3　TEM images of the La^{3+}-doped TiO_2 calcinated at 750 °C

Fig.4 HRTEM images and SAED patterns of the La^{3+}-doped TiO$_2$ calcinated at 750 °C

well known that the interfacial energy of the incoherent interface can be the lowest when the second phase precipitates as regular spheres. But the TiO$_2$ grain size gradually grows in the calcination process, which prevents the second phase to form regular spheres in the precipitation process. There are some distortions on the form of the precipitate.

2.3 Point defect thermodynamic model for grain boundary segregation

There are many different kinds of point defects in undoped or La^{3+}-doped TiO$_2$, such as intrinsic thermal, electronic, and non-stoichiometric ratio point defects, as indicated by the defect reactions summarized in Eqs.(4)~(7). Note that grain boundary segregation is, in fact, due to all kinds of point defects occurring at grain boundaries. The point defect distribution at a given TiO$_2$ grain boundary can be obtained using the defect reactions and point defect thermodynamics[16,17], as shown in Eqs.(8)~(11). Specifically, the defect concentrations of interstitial titanium and the titanium and oxygen vacancies are determined from the defect formation energy, the grain boundary electrostatic potential, and the temperature, as shown in Eqs.(8)~(10). In this work, by assuming that the defect formation energy is independent of the temperature, the actual defect formation energy should decrease with increased temperature[18,19]. The concentrations of acceptor-doping defects can be determined using Eq.(11), and are related to the doping concentration, static potential, and temperature. In particular, the concentration of the acceptor doping defect may be related to the elastic strain energy.
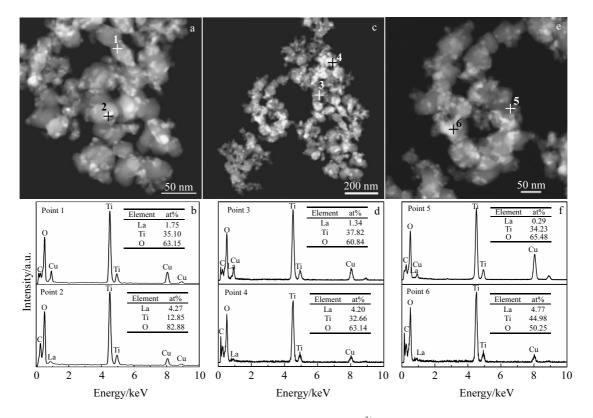

Fig.5 STEM images (a, c, e) and EDS results (b, d, f) of the La^{3+}-doped TiO$_2$ calcinated at 750 °C

Intrinsic thermal defects: $\text{null} \longleftrightarrow 2V_O^{\cdot\cdot} + V_{Ti}^{\prime\prime\prime\prime}$ (4)

Electronic defects: $\text{null} \longleftrightarrow e^\prime + h^\cdot$ (5)

Non-stoichiometric ratio point defects:

$$O_O \longleftrightarrow \frac{1}{2}O_2 + V_O^{\cdot\cdot} + 2e^\prime \qquad (6)$$

Acceptor La^{3+} doping defects:

$$2La_2O_3 \xleftarrow{\ TiO_2\ } 4La_{Ti}^\prime + Ti_i^{\cdot\cdot\cdot\cdot} + 8O_O^\times \qquad (7)$$

$$[Ti_i^{\cdot\cdot\cdot\cdot}](x) = \exp\left(-\frac{g_{Ti_i} + 4e\Phi(x)}{kT}\right) \qquad (8)$$

$$[V_{Ti}^{\prime\prime\prime\prime}](x) = \exp\left(-\frac{g_{V_{Ti}} - 4e\Phi(x)}{kT}\right) \qquad (9)$$

$$[V_O^{\cdot\cdot}](x) = 2\exp\left(-\frac{g_{V_O} + 2e\Phi(x)}{kT}\right) \qquad (10)$$

$$[La_{Ti}^\prime(x)] = C\exp\left[-\frac{e\Phi_\infty - e\Phi(x) - U_S^{La^{3+}}(x)}{kT}\right] \qquad (11)$$

In Eqs.(8)~(11), g_{Ti_i}, $g_{V_{Ti}}$, and g_{V_O} are the interstitial titanium, titanium vacancy, and oxygen vacancy formation energies, respectively, $e=1.602 \times 10^{-19}$ C is the electron charge, $\Phi(x)$ is the electrostatic potential at a distance of x from the grain boundary interface center, $k=1.381\times10^{-23}$ J·K^{-1} is the Boltzmann constant, T is the absolute temperature, $e\Phi(x)$ is the electrostatic potential energy at a distance of x from the grain boundary interface center, and Φ_∞ is the electrostatic potential in the grain when $\Phi(x)=0$. Further, $U_s(x)$ represents the elastic strain energy at a distance of x from the grain boundary interface center and C is the dopant concentration. All the terms on the left hand side in Eqs.(8)~(11) represent point defect concentration distributions.

For dopant ions with radii similar to that of Ti^{4+}, Φ acts as the segregation driving force. However, the radii of both La^{3+} (0.118 nm) are far larger than that of Ti^{4+} (0.068 nm), and so the elastic strain energy originating from the lattice mismatch U_0 cannot be ignored. The value of U_0 at the grain boundary interface center can be calculated using Eq.(12):

$$U_0 = \left(\frac{\Delta r}{r}\right)^2\left(3.45 - \frac{T}{1700}\right) \quad (eV) \qquad (12)$$

The elastic strain energy $U_0^{La^{3+}}$ in the La^{3+}-doped TiO_2 samples is 1.508 eV, as shown in Table 3.

The value of $U_s(x)$ can be calculated using Eq. (13):

$$U_s(x) = \begin{cases} U_0\left[1-(\frac{x}{2a})\right]^n & x \leqslant 2a \\ \\ 0 & x > 2a \end{cases} \qquad (13)$$

In Eq.(12), r is the Ti^{4+} radius in rutile TiO_2 lattices, Δr is the difference between the dopant ion radius and the Ti^{4+} radius in

Table 3   Elastic strain energy of the La^{3+}-doped TiO_2

Doping ion	Ti^{4+}	La^{3+}
Ionic radius, r/nm	0.068	0.118
Calcining temperature, T/°C	750	750
Elastic strain energy, U_0/eV		1.508

rutile TiO_2 lattices, and in Eq.(13), a is the lattice parameter of the rutile TiO_2 (here, a is the average value of a and c in the rutile TiO_2 lattice). When $x=0$, x represents the grain boundary interface center, and when $x=\infty$, it represents the grain interior. At that point, Φ_∞ is constant. The distribution $\Phi(x)$ can be obtained from Eq.(14):

$$\Phi(x)=\Phi_\infty[1-\exp(-x/\delta)] \qquad (14)$$

In Eq.(14), the Debye length δ indicates the shielding ability. The Debye length δ can be calculated from Eq.(15):

$$\delta = \left[\frac{\varepsilon_0 \varepsilon kT}{e^2 \sum N_i Z_i^2}\right] \qquad (15)$$

In Eq.(15), the vacuum dielectric constant ε_0 is 8.854×10^{-12} F·m^{-1} and the static TiO_2 dielectric constant ε is 120. N_i represents the concentration of each point defect i in the bulk phase per cubic centimeter, and Z_i represents the effective charges of each i in the bulk phase per cubic centimeter. As suggested by Eq. (14), $\Phi(x)$ is determined by δ and Φ_∞. Note that Φ_∞ is directly related to the defect formation energy, oxygen partial pressure, doping concentration, and temperature. Further, δ is determined by T, N_i, and Z_i. N_i and Z_i also are determined by the defect chemistry, oxygen partial pressure, doping, and other various factors. In this work, the point defect concentration distributions at the grain boundaries in the doped TiO_2 samples are calculated under 0.1 MPa pressure, for given calcining temperatures and doping concentrations.

For acceptor La^{3+} doping, the approximate electroneutrality condition in the TiO_2 bulk phase is expressed as

$$[La_{Ti}^\prime]_\infty = 4[Ti_i^{\cdot\cdot\cdot\cdot}]_\infty \qquad (16)$$

According to Eqs.(8), (11) and (16), Φ_∞ can be expressed as

$$e\Phi_\infty^{La_{Ti}^\prime} = -\frac{g_{Ti_i}}{4} - \frac{kT}{4}\ln\frac{[La_{Ti}^\prime]_\infty}{4} \qquad (17)$$

When the 5 mol% La-doped TiO_2 sample is calcined at 750 °C, the $[La_{Ti}^\prime]_\infty$ concentration is about 4.41 mol% for acceptor La^{3+} doping. The bulk phase electrostatic potential $\Phi_\infty^{La_{Ti}^\prime} = -0.514\ 89$ V can be obtained by substituting $g_{Ti_i} = 2$ eV, $[La_{Ti}^\prime]_\infty$, T, and k into Eq.(17). We can use $\Phi_\infty^{Ce_{Ti}^\prime} = -0.514\ 89$ V and Eqs.(15) and (16) to calculate $\Phi(x)$ at the grain boundaries. $\left[Ti_i^{\cdot\cdot\cdot\cdot}\right](x)$ and $[La_{Ti}^\prime](x)$ can be obtained by substituting $g_{Ti_i} = 2$ eV, $T = (750 + 273.15)$ K, and the La^{3+} doping concentration $C_{La^{3+}} = 4.41$ mol% into Eqs.(8) and (11), as shown in Fig.6a. From Fig.6a, we can see that the concentration of $[La_{Ti}^\prime]$ at the grain boundaries is very high. This shows that La can segregate strongly at grain boundaries, and this result is consistent with the XRD patterns, microstructure, EDS chemical composition analysis, and discuss in section 2.1 and 2.2. If U_0 is neglected, $[La_{Ti}^\prime](x)$ can be obtained according to Eq.(18), as shown in Fig.6b. From this figure, La segregation at the grain boundaries is not clearly observed. However, this is not in agreement with the

above experimental results. For dopant ions with radii similar to the Ti^{4+} radius, the grain boundary segregation driving force is the electrostatic potential. However, the La^{3+} ion radius of 0.118 nm is significantly larger than the Ti^{4+} ion radius of 0.068 nm; hence, U_0 cannot be ignored[20].

$$[La'_{Ti}(x)] = C_{La^{3+}} \exp[-\frac{e\Phi_{\infty} - e\Phi(x)}{kT}] \tag{18}$$

2.4 Chemical state analysis

Table 4 shows the atomic fractions of O 1s, Ti 2p and La 3d in the La^{3+}-doped TiO$_2$, which indicates the ratio between the atomic fractions of O 1s and Ti 2p in the La^{3+}-doped TiO$_2$ is far greater than 2. Therefore, there must be other forms of oxygen besides the combination with Ti. With the increase of the thermal processing temperature, the atomic fraction of O 1s gradually decreases, while that of La 3d gradually increases. When combined with the XRD measurements, it can be known that with the gradual increase of the thermal processing temperature, the adsorbed oxygen (for example, the surface hydroxyl and surface adsorbed water) gradually
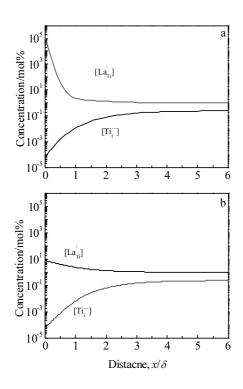

Fig.6   Point defect concentration distributions at grain boundaries in La-doped TiO$_2$ with (a) and without (b) elastic strain energy

Table 4   Atomic fraction of O 1s, Ti 2p and La 3d in the La^{3+}-doped TiO$_2$ (at%)

Calcination temperature/°C	100	550	750	900
O 1s	75.55	66.76	64.01	63.54
Ti 2p	23.89	30.66	31.68	29.02
La 3d	0.55	2.59	4.31	7.44

evaporates, which corresponds to the decrease of the O 1s signal, while partial La^{3+} precipitates as the second phase on the TiO$_2$ surface.

Fig.7a shows the fitted O 1s spectrum for the dry gel of the La^{3+}-doped TiO$_2$, which may be fitted as two peaks. The peak at E_b=530.25 eV belongs to the lattice oxygen of the Ti-O bond. The peak at E_b=532.84 eV belongs to the adsorbed oxygen that includes the surface hydroxyl and adsorbed water, most of which is the surface hydroxyl [21]. The O 1s spectra of the La^{3+}-doped TiO$_2$ after calcination at 550, 750, and 900 °C are shown in Fig.7b~7d, respectively. The peaks at E_b=530.36, 529.71, 530.36 eV originate from the lattice oxygen of the Ti-O, while those at E_b=528.82, 528.22, 528.82 eV come from the lattice oxygen of La-Ti-O. The peaks at E_b=532.39, 531.32 eV come from the adsorbed oxygen.

Table 5 shows the atomic fractions of the lattice oxygen and adsorbed oxygen of the La^{3+}-doped TiO$_2$ after thermal processing at different temperatures. It can be seen that the adsorbed oxygen of the La^{3+}-doped TiO$_2$ gradually disappears with the increase of the calcination temperature.

Fig.8 shows the fitted Ti 2p spectra of the La^{3+}-doped TiO$_2$, indicating the Ti 2p orbit is split into two energy states due to the spin-orbit interaction, namely, Ti 2p$_{1/2}$ and Ti 2p$_{3/2}$ [22]. It can be known from the fitting curve of the XPS spectrum that Ti^{3+} is generated in the La^{3+}-doped TiO$_2$ after calcination at 550 °C.

Table 6 shows the atomic fractions of Ti^{4+} and Ti^{3+} in the La^{3+}-doped TiO$_2$. It can be seen that the Ti ion only exists in the 4+ valence state in the La^{3+}-doped TiO$_2$ dry gel. However, with the increase of the calcination temperature, Ti ion contains two types of valence state Ti^{4+} and Ti^{3+} in the La^{3+}-doped TiO$_2$.

Fig.9 shows the fitted La 3d spectra of the La^{3+}- doped TiO$_2$. In Figs.9a~9d, the peaks at E_b=835.66, 835.52, 834.97, 834.99 eV correspond to the La 3d$_{5/2}$ of La^{3+}. It is also indicated that there is a so-called shake-up satellite peak (energy loss peak) besides the main peaks in the fitted La 3d spectra of La^{3+} 3d$_{5/2}$. A photoelectron will be emitted to the outer valence electron of the La element in photoionization, which is equivalently adding a nuclear charge on the outmost layer of the electrons of La. Therefore; there will be a relaxation process that causes the valence electrons to rearrange. The valence electron may transit to the unoccupied orbit, which is called a shake-up (carry) process. The process is shown as an energy loss peak on the higher binding energy side of the main peak in the fitted spectrum. Due to significant charge transfer between O and La in the La^{3+}-doped TiO$_2$, there are extra electrons on the 3d orbits of La and the intensity of the shake-up peak is very strong. In Figs.9a~9d, all the peaks at E_b=838.94, 838.75, 838.39, 838.94 eV are shake-up peaks of La^{3+}.

2.5 UV-Vis absorption spectrum analysis
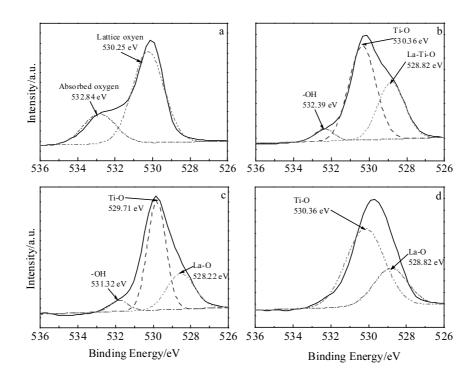
Fig.10 shows the UV-Vis absorption spectra of the samples,

Fig.7 Fitted O 1s spectra of the La^{3+}-doped TiO$_2$ at different calcination temperatures: (a) 100 °C, (b) 550 °C, (c) 750 °C, and (d) 900 °C

Table 5 Atomic fractions of the lattice oxygen and adsorbed oxygen of the La^{3+}-doped TiO$_2$ (at%)

Calcination temperature/°C	100	550	750	900
Ti-O	74.75	58.95	62.99	70.17
La-Ti-O	0	35.46	30.83	29.83
Absorbed oxygen	25.25	5.58	6.17	0

while their optical absorption band edges and band gaps are shown in Table 7. It can be known from Fig.10a and Table 7 that the optical absorption band edge of the un-doped TiO$_2$ is blue shifted and the band gap becomes wider with the increase of the calcination temperature. The un-doped TiO$_2$ has the best UV-Vis absorption with calcination at 400 °C. When connected with the XRD measurements, this phenomenon may be explained with the following reason. With the increase of the calcination temperature, the un-doped TiO$_2$ gradually changes from the anatase phase to the rutile phase. It is well known that there are a large number of lattice defects, as well as many dislocation networks in the anatase phase lattices. The degree of crystallization in the rutile phase is significantly better than that in the anatase phase. There are fewer lattice defects. Hence, the anatase phase has more oxygen holes to capture electrons, and the rutile phase is easier to promote the recombination of the photogenerated electron-hole pairs. Finally, the bandwidth of the UV-Vis absorption spectrum of the un-doped TiO$_2$ is narrowed with the changing of the anatase phase change to the rutile phase [23].

From Fig.10b and Table 7, it can be seen that with the increase of the calcination temperature, the optical absorption band edge of the La^{3+}-doped TiO$_2$ is blue shifted and the band gap becomes wider. It can be mainly explained with the following two reasons. Firstly, the La^{3+}-doped TiO$_2$ gradually changes from the anatase phase to the rutile phase with the increasing calcination temperature. There are less lattice defects and dislocation networks in the rutile phase lattice than in the anatase phase. It is easier for the photogenerated electron-hole pairs to recombine in the rutile phase, which causes the UV-Vis optical absorption band edge of the La^{3+}-doped TiO$_2$ to blue shift. Secondly, La^{3+} ions are precipitated in the form of La$_4$Ti$_9$O$_{24}$ on the TiO$_2$ surface with the increase of the calcination temperature. This second phase is enriched at the grain boundary and becomes the electron-hole recombination centers, which prevents the migration of electrons and holes towards the TiO$_2$ surface. It also destroys the integrity of the periodic potential field of the TiO$_2$ lattice, so do the TiO$_2$ crystal planes. It reduces the effective area of TiO$_2$ and is not beneficial to improve the range of the UV-Vis absorption of TiO$_2$ [24].

Table 7 also indicates that TiO$_2$ doped with La^{3+} red shifts the optical absorption band edge. This phenomenon can be explained with the following two reasons. On the one hand, the La^{3+}-doping generates doping defects in TiO$_2$, which is equivalent to introducing impurity energy levels and changes the TiO$_2$ band gap[25,26]. Indeed, it improves the distribution of the charges and carriers and leads to widening of the bandwidth of the UV-Vis absorption spectrum of TiO$_2$. On the other hand, it can be seen from the TEM observation that the dispersibility
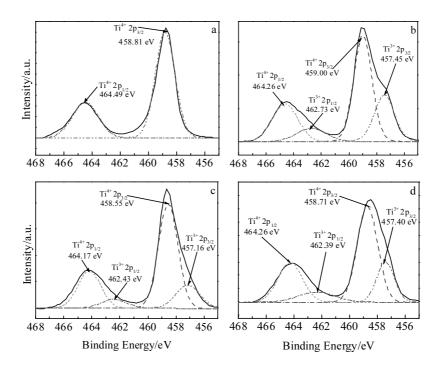
Fig.8   Fitted Ti 2p spectra of the La^{3+}-doped TiO$_2$ at different calcination temperatures: (a) 100 °C, (b) 550 °C, (c) 750 °C, and (d) 900 °C

Table 6   Atomic fractions of Ti^{4+} and Ti^{3+} in the La^{3+}-doped TiO$_2$ (at%)

Calcination temperature/°C	100	550	750	900
Ti^{4+}	100	67.96	77.98	73.22
Ti^{3+}	0	32.04	22.02	26.78

of the La^{3+}-doped TiO$_2$ is significantly better than that of the un-doped TiO$_2$. Hence, the effective area for optical absorption of the La^{3+}-doped TiO$_2$ increases, which widenes the UV-Vis absorption spectrum of TiO$_2$.
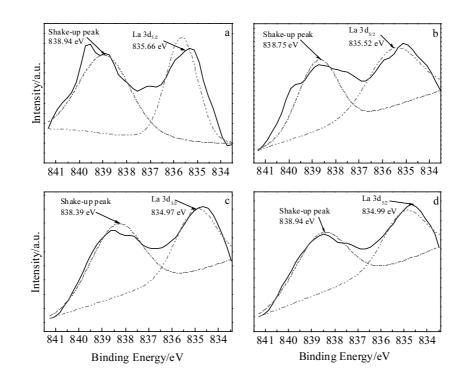

Fig.9   Fitted La 3d spectra of the La^{3+}-doped TiO$_2$ at different calcination temperatures: (a) 100 °C, (b) 550 °C, (c) 750 °C, and (d) 900 °C
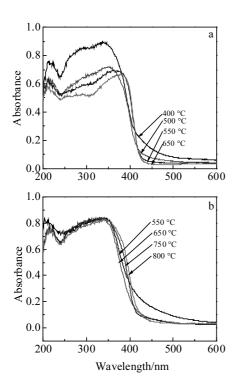
Fig.10   UV-Vis absorption spectra of TiO_2 (a) and La^{3+}-doped TiO_2 (b)

Table 7   Optical absorption band edge and band gap of the sample

Sample	Calcination temperature/°C	λ_g/nm	E_g/eV
TiO$_2$	400	430	2.8837
	500	428	2.8972
	550	426	2.9108
	650	424	2.9245
La^{3+}-TiO$_2$	550	435	2.8506
	650	426	2.9077
	750	423	2.9314
	800	422.7	2.9335

3   Conclusions

1) Doping with La^{3+} suppresses the phase transmission and grain growth of TiO_2, and the second phase $La_4Ti_9O_{24}$ precipitates after calcination at 750 °C.

2) The dispersibility of the La^{3+}-doped TiO_2 is significantly improved. Both grains growth and phase transformation from anatase phase to rutile phase of TiO_2 are suppressed by the pinning effect of second phase. The second phase $La_4Ti_{19}O_{24}$ gradually precipitates from the La^{3+}-doped TiO_2 and forms an incoherent interface with the brookite TiO_2 phase, which precipitates in the form of irregular spheres from the surface of the TiO_2 base.

3) The driving force of La^{3+} segregation is elastic strain energy. La^{3+} segregation in La^{3+}-doped TiO_2 is dominated by elastic strain energy. Secondary phase $La_4Ti_9O_{24}$ in La^{3+}-doped TiO_2 is initiated from segregation.

4) With the increase of calcination temperature, the atomic fraction of the O 1s in the La^{3+}-doped TiO_2 gradually decreases, and that of the La 3d gradually increases. There is an energy loss peak at the higher binding-energy side of the main peak of the La 3d, and Ti^{3+} exists after the calcination.

5) The ultraviolet-visible (UV-Vis) spectroscopy shows doping with La^{3+} red-shifts the optical absorption bandedge of the TiO_2. But with increasing the calcination temperature, the optical absorption bandedge blue shifts.

References

1   Mahsa Motegh, Ruud van Ommen J, Peter W Appel *et al. Environ Sci Technol*[J], 2014, 48(3): 1574

2   Lee Taek-Yong, Kim Hui-Seon, Park Nam-Gyu. *Chemphyschem*[J], 2014, 15: 1098

3   Feng Guangjian, Liu Suwen, Xiu Zhiliang *et al. Rare Metal Materials and Engineering*[J], 2009, 38(1): 185 (in Chinese)

4   Kernazhitsky L, Shymanovska V, Gavrilko T. *Journal of Solid State Chemistry*[J], 2013, 198: 511

5   Wang Jun, Li Ronghe, Zhang Zhaohong *et al. Inorganic Materials*[J], 2008, 44(6): 608

6   Du Jinghong, Yan Jikang, Zhang Jiamin *et al. Rare Metal Materials and Engineering*[J], 2015, 44(11): 2821 (in Chinese)

7   Yue Linghai, Shui Miao, Xu Zhude *et al. Journal of Zhejiang University, Sciences Edition*[J], 2000, 27(1): 69

8   Ranjit K T, Willner I, Bossmann S H *et al. Environ Sci Technol*[J], 2001, 35(7): 1544

9   Sekiya T, Ohta S, Kamei S *et al. Journal of Physics and Chemistry of Solids*[J], 2001, 62(4): 717

10   Li Minchi, Feng Cao, Li Xiang *et al. Rare Metal Materials and Engineering*[J], 2018, 47(S1): 379 (in Chinese)

11   Ranjana Verma, Samdarshi S K. *Journal of Alloys & Compounds*[J], 2015, 629: 105

12   Xu X H, Wang M, Hou Y *et al. Crystal Research & Technology*[J], 2002, 37(5): 431

13   Yan Jikang, Gan Guoyou, Du Jinghong *et al. Piezoelectrics & Acoustooptics*[J], 2011, 33(5): 779

14   Li tianduo, Li huali, Liu Haixia *et al. Rare Metal Materials and Engineering*[J], 2017, 46(2): 533 (in Chinese)

15   Xu Anwu, Gao Yuan, Liu Hanqin. *Journal of Catalysis*[J], 2002, 207(2): 151

16   Yan Jikang, Kang Kunyong, Du Jinghong *et al. Ceramics International*[J] 2016, 42(10): 11 584

17   Bataille A, Addad A, Courtois C *et al. J Euro Ceram Soc*[J], 2008, 28(6): 1129

18   He J, Behera R K, Finnis M W *et al. Acta Mater*[J], 2007, 55(13): 4325

19   Li X, Finnis M W, He J *et al. Acta Mater*[J], 2009, 57(19): 5882

20   Wang Q L, Lian G D, Elizabeth C. *Acta Mater*[J], 2004, 52(4): 809

21   Michael R Hoffann, Scot T Martin, Wonyong Choi *et al.*

Chemical Reviews[J], 1995, 95(1): 69

22 Yang Xiangxin, Cao Chundi, Hohn Keith *et al. Journal of Catalysis*[J], 2007, 252(2): 296

23 Bickley R I, Stone F S. *Journal of Catalysis*[J], 1973, 31(3): 389

24 Xie Yibing, Yuan Chunwei. *Applied Surface Science*[J], 2004,

221(1-4): 17

25 Maria Crişan, Mălina Răileanu, Nicolae Drăgan *et al. Applied Catalysis A: General*[J], 2015, 504(5): 130

26 Wang X H, Li J G, Kamiyama H *et al. J Am Chem Soc* [J], 2005, 127(31): 10 982

La^{3+}掺杂 TiO$_2$ 纳米粉体的相组成和光催化性能

严继康 [1]，荣雪荃 [2]，顾　鑫 [1]，杜景红 [1]，甘国友 [1]

(1. 昆明理工大学，云南 昆明 650093)

(2. 北京科技大学，北京 100083)

摘　要：采用溶胶-凝胶法制备了 La^{3+}掺杂 TiO$_2$。利用 XRD、TEM、HRTEM、STEM-EDS、XPS 和 UV-Vis 对样品进行表征，讨论 La^{3+}掺杂 TiO$_2$ 在相变过程中的物相组成、平均晶粒尺寸、微观结构、化学态和紫外-可见吸收光谱等方面的变化。结果表明，掺杂 La^{3+}明显地抑制了 TiO$_2$ 的相转变和晶粒长大，有效地改善了 TiO$_2$ 的分散性，并减小了 TiO$_2$ 的平均颗粒尺寸。随着煅烧温度升高，La^{3+}掺杂 TiO$_2$ 逐渐析出第二相 La$_4$Ti$_{19}$O$_{24}$，其会与 TiO$_2$ 板钛矿相形成非共格界面，并以不规则球体的形式在 TiO$_2$ 基体表面析出。第二相 La$_4$Ti$_{19}$O$_{24}$ 来源于点缺陷在 La 掺杂 TiO$_2$ 晶界的偏析，偏析驱动力主要是是弹性应变能。随着煅烧温度的升高，La^{3+}掺杂 TiO$_2$ 中 O 1s 的原子分数逐渐降低，La 3d 的原子分数逐渐升高，且 La 3d 主峰的高结合能端有一个能量损失峰，煅烧后存在 Ti^{3+}；掺杂 La^{3+}使 TiO$_2$ 的光吸收带边红移，但随着煅烧温度的升高，其光吸收带边蓝移。

关键词：二氧化钛；相变；镧；光催化

作者简介：严继康，男，1972 年生，博士，教授，昆明理工大学材料科学与工程学院，云南 昆明 650093，电话：0871-65109952，E-mail: scyjk@sina.com